GSA Data Repository 2020006

Alvaro, M., et al., 2020, Fossil subduction recorded by quartz from the coesite stability field: Geology, v. 48, https://doi.org/10.1130/G46617.1

SUPPLEMENTARY MATERIAL

METHODS

X-ray diffraction and Micro-Raman spectroscopy

As showed in Murri et al. (2018), we determined the unit-cell parameters of the inclusion by single-crystal X-ray diffraction measurements using the 8-position centering method by Angel and Finger(Angel and Finger, 2011) using a newly developed Huber 4-circle Eulerian cradle diffractometer equipped with point detector and microfocus source (120 μm spot size). On the same inclusion polarized Raman spectra were collected in backscattering geometry with a Horiba Jobin-Yvon T64000 triple-monochromator spectrometer (spectral resolution of ~2 cm^{-1}, instrumental accuracy in peak positions of ~0.35 cm^{-1} and 2 μm spot size) following the same protocol reported in Campomenosi et al. (2018).

Synchrotron X-ray microtomography

Non-destructive, high-resolution technique that produces three-dimensional maps of the variations of the X-ray attenuation coefficient within a given sample. X-ray micro-tomography experiments were carried out at the Swiss Light Source (SLS) at TOMCAT, a beamline for TOmographic Microscopy and Coherent rAdiology experimenTs (Stampanoni et al., 2006). Measurements were performed at 13.5 keV in order to maximize contrast. A total of 1501 X-ray radiographs were acquired from different angular positions around a vertical rotation axis for each sample. The used imaging setup consisted of a 20 μm thick LuAG:Ce scintillator screen, a 20× objective and a sCMOS (PCO.edge) camera. The tomographic reconstruction was performed using optimized routines based on the Fourier Transform Method (Marone and Stampanoni, 2012). The resulting volume consisted of 2160 axial slices of 2560 × 2560 pixels, with a pixel size of 0.33 μm.

Finite element modelling

The FE analysis was performed on the real 3D model built from the segmentation of the X-ray microtomographic data (Fig. 1). The surface of the model was smoothed to improve the quality of the final FE mesh and the final 3D model was then assembled placing the two inclusions in the garnet host. An elastically isotropic analysis was run with Simulia Abaqus, a commercial engineering package for FE analysis (for more details see Mazzucchelli et al. 2018). For the quartz inclusions we used the isothermal bulk modulus from the Equation of State (EoS) as reported in Angel et al. (2017a). For garnet we used the isothermal bulk modulus from the P-V-T EoS reported by (Milani et al., 2017; Milani et al., 2015) and the shear modulus reported by Milani et al. (2015).

How to determine entrapment conditions on anisotropic inclusions in cubic host

The strain along the crystallographic *a*-axis of an inclusion crystal measured as a_i can be defined as,

$$\varepsilon_1 = (a_i - a_0)/a_0 \qquad \text{(M1)}$$

Where a_0 is the unit-cell parameter the inclusion crystal would have when it is free from the host and at room pressure and temperature. In general, strain is a second rank tensor with six components(Nye, 1985). The three normal components (ε_1, ε_2 and ε_3 in Voigt notation) describe the change in dimensions in three mutually perpendicular directions in the inclusion, and for crystals with orthorhombic symmetry and higher can be defined purely in terms of the cell parameters *a*, *b*, and *c*, as in equation (M1). Three shear components (ε_4, ε_5 and ε_6) characterise the strains in three mutually-perpendicular planes. For uniaxial inclusion crystals such as quartz, trapped inside approximately isotropic garnet host crystals, the shear strains are too small to be measured at the centre of the inclusion, and can be ignored. Equation (M1)

defines the Lagrangian infinitesimal strains, which are usually suitable for the analysis of the remanent strains in inclusions when the host is at room conditions because the strains are small.

Once the measured inclusion pressure or strain (as appropriate) has been corrected for the effects of mutual relaxation including the influence of shape and other geometric factors, the determination of possible entrapment is a purely thermodynamic calculation using the equations of state and/or the known variation of the cell parameters of both host and inclusion phases with temperature and pressure. By first introducing the method for cubic inclusions we show that the two methods are conceptually and algebraically identical.

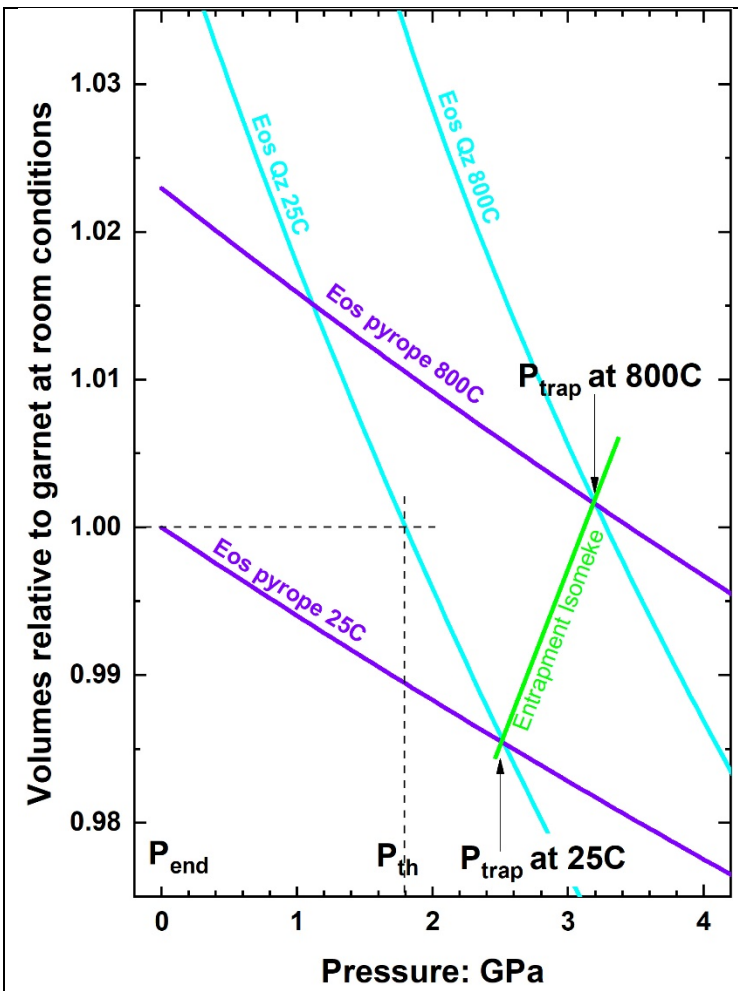

Figure M1: Volume equations of state for pyrope and quartz to illustrate the principles of the calculation of an entrapment isomeke for isotropic systems. When the host/inclusion system is at room conditions, the quartz inclusion has the same volume as the pyrope host, and is therefore under a pressure P_{th} ~1.8 GPa in this example, if relaxation is not taken into account. The EoS of quartz shows that a free quartz crystal would have a volume of 1.043 on this scale. Cold compression of the quartz and the pyrope independently would bring them to the same *T, V* and *P* at ~2.53 GPa, which defines one point of possible entrapment. At 800°C the EoS of quartz and pyrope show that they cross at ~3.2 GPa. The locus of such points at different temperatures defines the entrapment isomeke for an isotropic system.

When the host is at the final external pressure and temperature P_{end} and T_{end}, the inclusion is constrained to the volume of the cavity within the host at these conditions. We will call this cavity volume

$V_{host}(P_{end}, T_{end})$. The pressure P_{th} in the inclusion is determined by the EoS of the inclusion and this volume and the same temperature T_{end}. Now consider the effects of an increase in pressure on the two minerals separately. If the host is a stiff garnet, and the inclusion is soft like quartz, a free quartz crystal will decrease in volume faster than the volume of the cavity in the host (Fig M1). At a certain pressure the volume of a free quartz crystal and the cavity will become equal, and the quartz will fit into the cavity without any further compression. Therefore, there will not be any pressure gradient across the system. The system has uniform hydrostatic *P* and *T*, and these are one possible set of conditions of entrapment. It is clear from Fig M1 that the entrapment pressure is defined by the condition for which the fractional volume change for the two phases from entrapment to the final conditions is the same. Thus:

$$\frac{V_{host}(P_{trap}, T_{trap})}{V_{host}(P_{end}, T_{end})} = \frac{V_{inc}(P_{trap}, T_{trap})}{V_{inc}(P_{th}, T_{end})} \qquad \text{(M2)}$$

The same calculation can be performed for any chosen T_{trap} with the normal EoS of the phases to find the pressure at which the volume of the cavity matches the volume of the free inclusion phase (Fig M1). The locus of such points defined by equation (M2) is the entrapment isomeke. Entrapment conditions are therefore also defined in equation M2 as states where there are no strain gradients across the host and inclusion. We note that the incorporation of the volume change due to relaxation into this calculation is not correct, and leads to incorrect values of entrapment pressures(Guiraud and Powell, 2006).

For isotropic and cubic materials the cube-root of the volume change is equal to the change in linear dimensions, so Equation (M2) can also be written as:

$$\left[\frac{V_{host}(P_{trap}, T_{trap})}{V_{host}(P_{end}, T_{end})}\right]^{1/3} = \left[\frac{V_{inc}(P_{trap}, T_{trap})}{V_{inc}(P_{th}, T_{end})}\right]^{1/3} \qquad \text{(M3)}$$

This emphasizes that the conditions for entrapment are that the linear dimensions of the free host and inclusion crystals must be equal at the time of entrapment in order to avoid stress or strain gradients across the system. Thus, the entrapment isomeke is equally-well described as the locus of *P, T* conditions

along which no strain gradients are developed in elastically isotropic host-inclusion systems. If the inclusion phase is non-cubic, the entrapment conditions are therefore defined for each crystallographic axis a_i by:

$$\left[\frac{V_{host}(P_{trap}, T_{trap})}{V_{host}(P_{end}, T_{end})}\right]^{1/3} = \frac{a_{i,inc}(P_{trap}, T_{trap})}{a_{i,inc}(P_{th}, T_{end})} \quad \text{(M4)}$$

The crystallographic lengths $a_{i,inc}(P_{th}, T_{end})$ of the inclusion are obtained from the measured strains ε_i corrected for relaxation. For uniaxial inclusion crystals such as quartz, the expressions for the *a* and *b* axes are identical (because the symmetry of the inclusion is not broken by a cubic host mineral). If the variation of unit-cell parameters of the inclusion with *P* and *T* are known, then each of the *a* and *c* axes allows a line of possible entrapment conditions to be calculated from Eqn M4. The intersection of these two lines (e.g. Fig. 2b, main text) provides a unique *P* and *T* of entrapment from each individual inclusion.

Axial equations of state for quartz

In order to implement this new method of calculating entrapment conditions from measurement of the axial strains of the inclusion crystal, it is necessary to have a description of how the unit-cell parameters of a free crystal change with temperature and hydrostatic pressure. We determined the parameters for the 'linear equation of state' of the *a*-axis of quartz in the same way as previously reported for the volume EoS (Angel et al., 2017a). Quartz undergoes a displacive phase transition between the alpha and beta phases at high temperatures, so the EoS of both the volumes and the cell parameters is comprised of three components; the EoS of the 'bare' beta phase, the excess properties due to the phase transition to the alpha phase, and an equation describing the position of the boundary in *P* and *T* (Angel et al., 2017a). We used the same

curved model for the phase boundary as in the volume EoS. The remaining parameters of the EoS for the *a*-axis were determined by simultaneous fitting with EosFit7 (Angel et al., 2014a) to the unit-cell data and linear compressibilities (from elastic tensor determinations) from exactly the same sources as used for the volume EoS. The '.eos' file which can be used with the EosFit7 program suite with the parameters describing the *P*,*T* variation of the *a*-axis of quartz is provided as part of the supplementary materials.

The same procedure could also be applied to the unit-cell parameter *c*, but the small misfits to the data and correlation between the EoS parameters then means that the values of *a, c* and *V* obtained from the three EOS are not 100% consistent at all *P* and *T*, i.e. that sometimes $a^2c.cos30 \neq V$. Therefore, in order to maintain 100% consistency in both the cell parameter values at all *P* and *T* conditions (which correspond to the strains) and all of their pressure derivatives (corresponding to the thermal expansion and compressibility tensors (Zaffiro et al., 2019), we use the EoS for the volume and the *a*-axis of quartz, and calculate all values of *c* from them as $c = \frac{V}{a^2 cos30}$. As an example, we provide in Fig. M2 a comparison to measured data of the temperature variation of the *a*- and *c*-unit-cell parameters of quartz calculated from the two EoS for *a* and *V*. The misfit below room temperature is due to order-parameter saturation (Angel et al., 2017a; Salje et al., 1991) which is not included in the models, and data below 200 K were therefore not used in the fits.

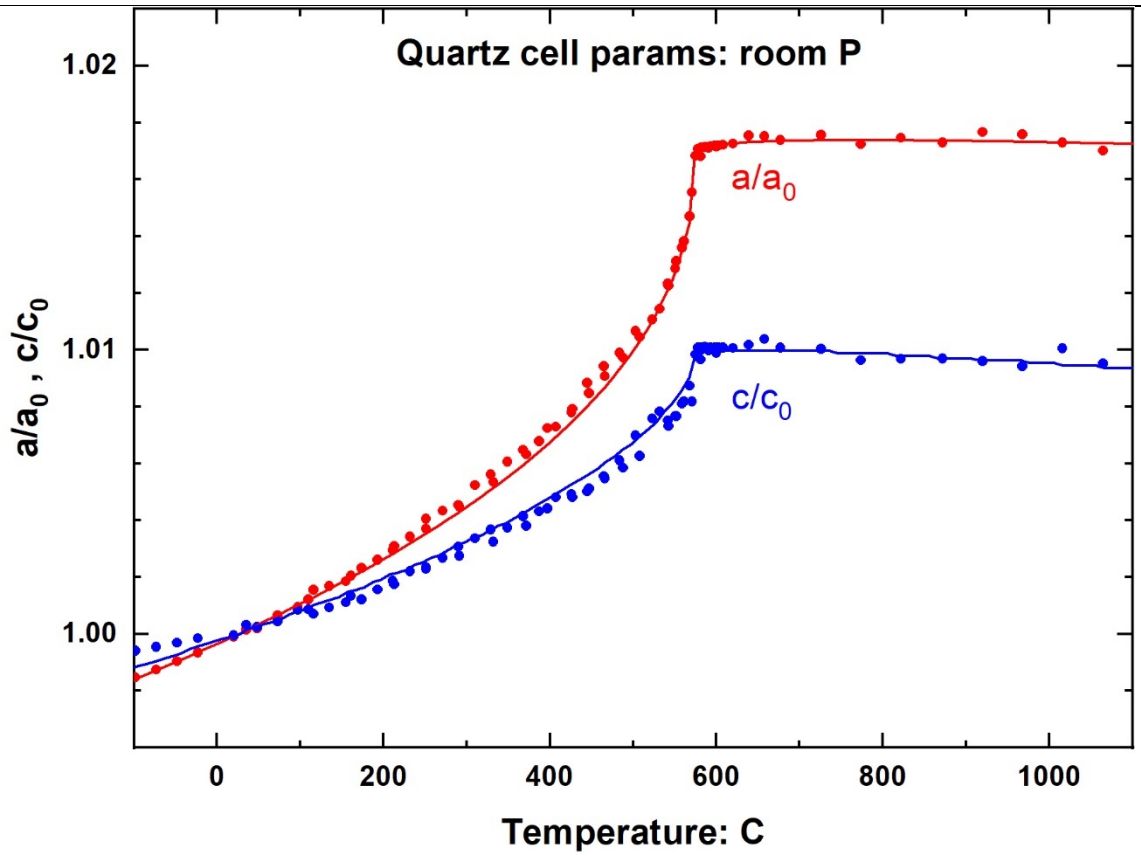

Figure M2: Cell parameter variation of quartz with temperature. Points are data from Carpenter *et al*(Carpenter et al., 1998). The red line is the axial EoS for the quartz *a* cell parameter, and the blue line are the values of the *c*-cell parameter calculated from the volume EoS(Angel et al., 2017a), and the axial EoS for the *a*-axis.

References

Angel, R. J., Alvaro, M., Miletich, R., and Nestola, F., 2017a, A simple and generalised P–T–V EoS for continuous phase transitions, implemented in EosFit and applied to quartz: Contributions to Mineralogy and Petrology, v. 172, no. 5, p. 29-29.

Angel, R. J., and Finger, L. W., 2011, SINGLE: a program to control single-crystal diffractometers: Journal of Applied Crystallography, v. 44, no. 1, p. 247-251.

Angel, R. J., Gonzalez-Platas, J., and Alvaro, M., 2014a, EosFit7c and a Fortran module (library) for equation of state calculations: Zeitschrift Fur Kristallographie-Crystalline Materials, v. 229, no. 5, p. 405-419.

Angel, R. J., Mazzucchelli, M. L., Alvaro, M., and Nestola, F., 2017b, EosFit-Pinc: A simple GUI for host-inclusion elastic thermobarometry: American Mineralogist, v. 102, no. 9, p. 1957-1960.

Angel, R. J., Mazzucchelli, M. L., Alvaro, M., Nimis, P., and Nestola, F., 2014b, Geobarometry from host-inclusion systems: The role of elastic relaxation: American Mineralogist, v. 99, no. 10, p. 2146-2149.

Angel, R. J., Murri, M., Mihailova, B., and Alvaro, M., 2019, Stress, strain and Raman shifts: Zeitschrift fur kristallograhie - Crystalline Material, v. 234, no. 2, p. 11.

Angel, R. J., Nimis, P., Mazzucchelli, M. L., Alvaro, M., and Nestola, F., 2015, How large are departures from lithostatic pressure? Constraints from host-inclusion elasticity: Journal of Metamorphic Geology, v. 33, no. 8, p. 801-813.

Aulbach, S., Jacob, D., Cartigny, P., Stern, R., Simonetti, S., Wörner, G., and Viljoen, K., 2017, Eclogite xenoliths from Orapa: Ocean crust recycling, mantle metasomatism and carbon cycling at the western Zimbabwe craton margin: Geochimica et Cosmochimica Acta, v. 213, p. 574-592.

Campomenosi, N., Mazzucchelli, M. L., Mihailova, B. D., Scambelluri, M., Angel, R. J., Nestola, F., Reali, A., and Alvaro, M., 2018, How geometry and anisotropy affect residual strain in host inclusion system: coupling experimental and numerical approaches: American Mineralogist, v. 103, no. 12, p. 2032-2035.

Carpenter, M. A., Salje, E. K. H., Graeme-Barber, A., Wruck, B., Dove, M. T., and Knight, K. S., 1998, Calibration of excess thermodynamic properties and elastic constant variations associated with the alpha <->beta phase transition in quartz: American Mineralogist, v. 83, no. 1-2, p. 2-22.

Eshelby, J. D., 1957, The determination of the elastic field of an ellipsoidal inclusion, and related problems: Proceedings of the Royal Society of London, Series A; Mathematical and Physical Sciences, v. 241, no. 1226, p. 376-396.

Ferrero, S., and Angel, R. J., 2018, Micropetrology: Are Inclusions Grains of Truth?: Journal of Petrology.

Griffin, W. L., and O'Reilly, S. Y., 2007, Cratonic lithospheric mantle: is anything subducted?

Guiraud, M., and Powell, R., 2006, P–V–T relationships and mineral equilibria in inclusions in minerals: Earth and Planetary Science Letters, v. 244, no. 3, p. 683-694.

Howell, D., Wood, I. G., Dobson, D. P., Jones, A. P., Nasdala, L., and Harris, J. W., 2010, Quantifying strain birefringence halos around inclusions in diamond: Contributions to Mineralogy and Petrology, v. 160, no. 5, p. 705-717.

Korsakov, A. V., Hutsebaut, D., Theunissen, K., Vandenabeele, P., and Stepanov, A. S., 2007, Raman mapping of coesite inclusions in garnet from the Kokchetav Massif (Northern Kazakhstan): Spectrochimica Acta - Part A: Molecular and Biomolecular Spectroscopy, v. 68, no. 4, p. 1046-1052.

Korsakov, A. V., Zhukov, V. P., Perraki, M., and De Gussem, K., 2009, Is quartz a potential indicator of ultrahigh pressure metamorphism? Laser Raman spectroscopy of quartz inclusions in ultrahigh-pressure garnets: European Journal of Mineralogy, v. 21, p. 10.

Kotková, J., O'Brien, P. J., and Ziemann, M. A., 2011, Diamond and coesite discovered in Saxony-type granulite: Solution to the Variscan garnet peridotite enigma: Geology, v. 39, no. 7, p. 667-670.

Litasov, K. D., Malkovets, V. G., Kostrovitsky, S. I., and Taylor, L. A., 2003, Petrogenesis of ilmenite-bearing symplectite xenoliths from vitim alkaline basalts and yakutian kimberlites, Russia: International Geology Review, v. 45, no. 11, p. 976-997.

Marone, F., and Stampanoni, M., 2012, Regridding reconstruction algorithm for real-time tomographic imaging: Journal of Synchrotron Radiation, v. 19, no. 6, p. 1029-1037.

Mazzucchelli, M. L., Burnley, P., Angel, R. J., Morganti, S., Domeneghetti, M. C., Nestola, F., and Alvaro, M., 2018, Elastic geothermobarometry: Corrections for the geometry of the host-inclusion system: Geology, v. 46, no. 3, p. 231-234.

Mazzucchelli, M. L., Morganti, S., Reali, A., Chiara Domeneghetti, M., Angel, R. J., and Alvaro, M., 2019, Elastic geobarometry: relaxation of elastically anisotropic inclusions.

Milani, S., Angel, R. J., Scandolo, L., Mazzucchelli, M. L., Ballaran, T. B., Klemme, S., Domeneghetti, M. C., Miletich, R., Scheidl, K. S., Derzsi, M., Tokar, K., Prencipe, M., Alvaro, M., and Nestola, F., 2017, Thermo-elastic behavior of grossular garnet at high pressures and temperatures: American Mineralogist, v. 102, no. 4, p. 851-859.

Milani, S., Nestola, F., Alvaro, M., Pasqual, D., Mazzucchelli, M. L., Domeneghetti, M. C., and Geiger, C. A., 2015, Diamond-garnet geobarometry: The role of garnet compressibility and expansivity: Lithos, v. 227, p. 140-147.

Murri, M., Alvaro, M., Angel, R. J., Prencipe, M., and Mihailova, B. D., 2019, The effects of non-hydrostatic stress on the structure and properties of alpha-quartz: Physics and Chemistry of Minerals.

Murri, M., Mazzucchelli, M. L., Campomenosi, N., Korsakov, A. V., Prencipe, M., Mihailova, B. D., Scambelluri, M., Angel, R. J., and Alvaro, M., 2018, Raman elastic geobarometry for anisotropic mineral inclusions: American Mineralogist, v. 103, no. 11, p. 1869-1872.

Nye, J. F., 1985, Physical Properties of Cristals: Their Representation by Tensors and Matrices, Oxford University Press.

Pollack, H. N., and Chapman, D. S., 1977, On the regional variation of heat flow, geotherms, and lithospheric thickness: Tectonophysics, v. 38, no. 3-4, p. 279-296.

Rosenfeld, J. L., and Chase, a. B., 1961, Pressure and temperature of crystallization from elastic effects around solid inclusions in minerals?, Volume 259, p. 519-541.

Salje, E. K. H., Wruck, B., and Thomas, H., 1991, Order-parameter saturation and low-temperature extension of Landau theory: Zeitschrift für Physik B Condensed Matter, v. 82, no. 3, p. 399-404.

Schertl, H.-P., Schreyer, W., and Chopin, C., 1991, The pyrope-coesite rocks and their country rocks at Parigi, Dora Maira Massif, Western Alps: detailed petrography, mineral chemistry and PT-path: Contributions to Mineralogy and Petrology, v. 108, no. 1-2, p. 1-21.

Shimizu, N., and Sobolev, N., 1995, Young peridotitic diamonds from the Mir kimberlite pipe: Nature, v. 375, no. 6530, p. 394.

Spear, F. S., and Pattison, D. R., 2017, The implications of overstepping for metamorphic assemblage diagrams (MADs): Chemical Geology, v. 457, p. 38-46.

Stampanoni, M., Groso, A., Isenegger, A., Mikuljan, G., Chen, Q., Bertrand, A., Henein, S., Betemps, R., Frommherz, U., and Böhler, P., Trends in synchrotron-based tomographic imaging: the SLS experience, *in* Proceedings Developments in X-ray Tomography V2006, Volume 6318, International Society for Optics and Photonics, p. 63180M.

Taylor, L. A., Snyder, G. A., Keller, R., Remley, D. A., Anand, M., Wiesli, R., Valley, J., and Sobolev, N. V., 2003, Petrogenesis of group A eclogites and websterites: evidence from the Obnazhennaya kimberlite, Yakutia: Contributions to Mineralogy and Petrology, v. 145, no. 4, p. 424-443.

Tomilenko, A. A., Kovyazin, S. V., and Pokhilenko, N. P., Primary crystalline and fluid inclusions in garnet from diamondiferous eclogite from kimberlite pipes Mir and Udachnaya, Yakutiya, Russia, *in* Proceedings 'ECROFI XVIII. European current research on fluid inclusions, Siena, Italy, 2005/7/6-9 2005.

Zaffiro, G., Angel, R. J., and Alvaro, M., 2019, Constraints on the Equations of State of stiff anisotropic minerals: rutile: Mineralogical Magazine.

Zhang, Y., 1998, Mechanical and phase equilibria in inclusion–host systems: Earth and Planetary Science Letters, v. 157, no. 3–4, p. 209-222.

Zhong, X., Moulas, E., and Tajcmanova, L., 2018, Tiny timekeepers witnessing high-rate exhumation processes: Scientific Reports, v. 8, no. 1, p. 2234.
Zhukov, V. P., and Korsakov, A. V., 2015, Evolution of host-inclusion systems: A visco-elastic model: Journal of Metamorphic Geology, v. 33, no. 8, p. 815-828.

Acknowledgment

This project received funding from the European Research Council under the European Union's Horizon 2020 research and innovation program grant agreement n. 714936 (ERC-STG TRUE DEPTHS) to M. Alvaro. We acknowledge the Paul Scherrer Institut, Villigen, Switzerland for provision of synchrotron radiation beamtime at the TOMCAT beamline of the SLS.

Author contribution

MA, RJA, MS together devised and coordinated different aspects of the overall study. Raman experiments NC, M Murri; Sample characterization AK, AT; micro-tomography data collection and analysis FM, M Morana; Finite Element Models MLM; interpretation MA RJA MS FN. All authors participated in discussion of the results.